HHS Public Access

Author manuscript

Int J Hyperthermia. Author manuscript; available in PMC 2018 March 28.

Published in final edited form as:

Int J Hyperthermia. 2018 February ; 34(1): 19–29. doi:10.1080/02656736.2017.1317845.

Galectin-1-based tumour-targeting for gold nanostructure-mediated photothermal therapy

Samir V. Jenkins[a], **Dmitry A. Nedosekin**[b], **Emily K. Miller**[c], **Vladimir P. Zharov**[b,iD], **Ruud P. M. Dings**[a,iD], **Jingyi Chen**[c,iD], and **Robert J. Griffin**[a,iD]

[a]Department of Radiation Oncology, University of Arkansas for Medical Sciences, Little Rock, AR, USA

[b]Otolaryngology and Phillips Classic Laser and Nanomedicine Laboratories, University of Arkansas for Medical Sciences, Little Rock, AR, USA

[c]Department of Chemistry and Biochemistry, University of Arkansas, Fayetteville, AR, USA

Abstract

Purpose—To demonstrate delivery of Au nanocages to cells using the galectin-1 binding peptide anginex (Ax) and to demonstrate the value of this targeting for selective *in vitro* photothermal cell killing.

Materials and methods—Au nanocages were synthesised, coated with polydopamine (PDA), and conjugated with Ax. Tumour and endothelial cell viability was measured with and without laser irradiation. Photoacoustic (PA) mapping and PA flow cytometry were used to confirm cell targeting *in vitro* and in tissue slices *ex vivo*.

Results—Cell viability was maintained at ≥50% at 100 pM suggesting low toxicity of the nanocage alone. Combining the targeted construct (25 pM) with low power 808 nm laser irradiation for 10–20 min (a duration previously shown to induce rapid and sustained heating of Au nanocages [AuNC] in solution), resulted in over 50% killing of endothelial and tumour cells. In contrast, the untargeted construct combined with laser irradiation resulted in negligible cell killing. We estimate approximately 6×10^4 peptides were conjugated to each nanocage, which also resulted in inhibition of cell migration. Binding of the targeted nanocage reached a plateau after three hours, and cell association was 20-fold higher than non-targeted nanocages both *in vitro* and *ex vivo* on tumour tissue slices. A threefold increase in tumour accumulation was observed in preliminary *in vivo* studies.

CONTACT Robert J. Griffin rjgriffin@uams.edu Department of Radiation Oncology, University of Arkansas for Medical Sciences, 4301 W. Markham, Mail Slot #771, Little Rock, AR 72205, USA.

ORCID

Vladimir P. Zharov http://orcid.org/0000-0003-4773-0548

Ruud P. M. Dings http://orcid.org/0000-0001-7686-1331

Jingyi Chen http://orcid.org/0000-0003-0012-9640

Robert J. Griffin http://orcid.org/0000-0002-3574-2958

Supplemental data for this article can be accessed here.

Disclosure statement

The authors declare no conflicts of interest.

Conclusions—These studies demonstrate Ax's potential as an effective targeting agent for Au-based theranostics to tumour and endothelial cells, enabling photothermal killing. This platform further suggests potential for multimodal *in vivo* therapy via next-generation drug-loaded nanocages.

Keywords

Targeted nanomedicine; breast cancer; photothermal; photoacoustic microscopy; gold nanocage

Introduction

A handful of Au-nanoparticle-based therapeutics have recently entered pilot clinical studies against cancer [1–4], and a variety of preclinical systems are under intense investigation in laboratories across the globe [5,6]. Many of these nanotechnology-based systems rely on the enhanced permeability and retention (EPR) effect, by which nanoparticles passively accumulate in the tumour interstitium due to both extravasation and poor lymphatic clearance of tumours [7]. However, most studies show accumulation in the tumour of 1% or less of the injected dose [8]; the majority of injected materials accumulate in the liver and spleen [9,10]. Recent work has further shown that the pathophysiology of the tumour itself affects the uptake of nanoparticles [11]. The biodistribution of injected particles is highly dependent on their size, shape, and surface chemistry [12,13]. Use of targeting agents has shown the capacity to affect the tumour uptake and clearance rates of these particles [14], which can potentially reduce toxicity, costs, and other adverse effects. A variety of targeting agents have been conjugated to nanoparticles to direct them to specific proteins overexpressed on the cell surface of particular tumour types [15].

Targeting specific cells further increases the time that nanomaterials associate within/on the cell and tissue of interest, better localising therapeutic efficacy as the particles do not passively reside in the tumour interstitium [16] but rather bind to and/or are internalised by cells. For instance, targeted Au nanorods showed much greater ability to radiosensitize cells relative to untargeted particles despite roughly equivalent accumulation of the particles in an *in vivo* prostate cancer model [17]. In another study, polydopamine (PDA) coated Au nanorods were conjugated with anti-MUC1, which enabled selective photothermal killing of MUC1 overexpressing cells *in vitro* [18]. Similarly, we recently demonstrated the use of drug-loaded, targeted, PDA coated Au nanocages (AuNCs) for the eradication of established *S. aureus* biofilms [19]. Photothermal killing of bacterial cells was augmented with antibiotic delivery, and the close association between the offending cells and the nanotherapeutic was critical for the efficacy of the construct, which emphasises the importance of targeting in increasingly complex environments. This approach was adapted for tumour cell killing in part because of the strong photothermal capacity of AuNCs [20,21]. Indeed, the robust optical properties of the AuNCs, specifically the large absorption cross-section [22] and sensitivity of the localised surface plasmon resonance (LSPR) [23], guided its selection as the core particle. The PDA coating was added to enhance biocompatibility [24,25], enable drug loading [26], and provide a readily accessible functional handle for the conjugation of the targeting moiety [27].

While targeting tumour cells shows great promise for enhancing nanoparticle therapeutics, there is an extensive network of vasculature that supports these cells within a tumour. This vasculature is actively proliferating to provide new vessels that supply the growing tumour with nutrients [28], and studies suggest that the dividing vasculature is the limiting factor in tumour growth [29]. Targeting these dividing vascular cells to promote extravasation of the particles into the tumour parenchyma and damage the tumour vasculature is critical for effective use of nanoscale particles since they are unable to effectively penetrate the tumour microenvironment by passive means due to the tumour physiology. Indeed there are several endothelial specific vaccines that are in early stage clinical trials [30], with the goal being to educate the immune system to eradicate the rapidly dividing vasculature within the tumour. Tumour endothelial cells are also under investigation as a target for radiation [31–33] and chemotherapy [34] and we have demonstrated potent therapeutic effects using a vascular targeted gold nanoparticle in recent work [35–38].

Anginex (Ax) is an amphipathic synthetic 33-mer (3.6 kDa) that binds to galectin-1 [39], which plays an important role in cell division, adhesion, and migration. Important to the need for both effective delivery and therapeutic effect, galectin-1 is overexpressed by certain tumour cells and proliferating endothelial cells [40,41], and it is up-regulated by many stressors, including chemotherapy, radiation, and hypoxia [42,43]. Ax has been demonstrated to interfere with galectin-1's biological functions and inhibit cell proliferation [44–46]. Ax has further been shown to inhibit tumour angiogenesis and subsequent tumour growth [47–49]. Due to its structural stability and capacity to bind to both tumour and proliferating endothelial cells, Ax presents itself as a potent tumour microenvironment targeting agent that can bring a therapeutic agent to the tumour microvasculature and facilitate extravasation and activity [44,50,51].

In this work, Ax was used as a targeting agent to induce AuNC-mediated photothermal killing of tumour and endothelial cells. AuNCs were coated with PDA, isolated, and conjugated with Ax on the order of 60,000 peptides per AuNC. Ax was chosen for association with both tumour and endothelial cells, and the biological activity of Ax was retained after conjugation with AuNCs. 808nm laser-induced heating was used to kill both tumour and endothelial cells *in vitro*. Photothermal killing was only effective when the targeting agent was present on the AuNCs. *In vitro* binding to cells was further investigated using photoacoustic (PA) microscopy and PA flow cytometry. Mass analysis was performed to quantify the particle association with cells. These methods were then applied to validate that these particles target tumour tissue. Collectively, these data demonstrate the potency of using Ax as a targeting agent for photothermal treatment of tumour tissue and the potential of Ax-based photothermal nanomedicine to augment or replace other treatment modalities.

Materials and methods

Synthesis of PDA coated AuNCs (AuNC@PDA)

The AuNCs were synthesised by the galvanic replacement reaction between Ag nanocubes and $HAuCl_4$ as previously described [52] and fully detailed in the Supporting Information. AuNC@PDA was prepared by self-polymerization of dopamine on the surface of AuNCs under basic conditions in the presence of O_2 as previously described [19]. Briefly, 3 ml of 5

nM AuNC aqueous suspension was diluted to 200 ml using Tris-buffered saline (20 mM Tris and 100 mM NaCl, pH = 9) in a 250-ml, 3-neck, round-bottom flask. The reaction flask was briefly flushed with O_2 and placed in a bath sonicator held at 4°C with ice. Dopamine hydrochloride (0.2 mmol, 36.0 mg) was added to the flask, the vessel was sealed under 1 atm O_2, and the mixture was sonicated throughout the reaction until the extinction peak of AuNC had red-shifted ~30 nm (~60 min). The reaction was quenched by addition of 100 μL concentrated acetic acid. After this reaction, the product was collected by centrifugation at 6000 rcf for 10 min, washed with H_2O twice and recovered by centrifugation at 17,000 rcf for 10 min at 4°C. The AuNC@PDA was resuspended in H_2O at a concentration of 6 nM for characterisation and future use. Transmission electron microscopy (TEM) images were acquired using a JEM-1011 (Jeol). Optical absorption spectra were recorded using a UV–vis spectrometer (Cary 50, Agilent). The elemental analysis was performed using an inductively coupled plasma mass spectrometer (ICP-MS; iCAP Q, Thermo Scientific, Waltham, MA).

Anginex conjugation

Anginex was synthesised and purified as previously described [49]. Ax was conjugated to the surface of AuNC@PDA through the N-terminal amine and lysines by Michael addition to form AuNC@PDA-Ax [27]. Briefly, 1 nM AuNC@PDA were dispersed in 1 ml of 10 mM borate buffer (pH = 9) and 100 μg/mL of Ax was added to the solution. The reaction was allowed to proceed at 4°C overnight. The conjugates were collected and washed three times with H_2O by centrifugation at 19,000 rcf for 5 min at 4°C. The conjugates were dispersed in H_2O for future use and stored at 4°C. Conjugation efficiency was determined by Bradford assay of the first supernatant using various concentrations of AuNCs. The hydrodynamic radius of each preparation was assessed using a Particle Metrix nanoparticle sizing and distribution system (Particle Metrix GmbH, Germany). Particles were routinely analysed in this system at 1000 × dilution in LC water. Colloidal stability was assessed by monitoring the absorbance at the LSPR maximum over time, in the absence of agitation, following dispersion of 100 pM AuNC@PDA or AuNC@PDA-Ax in H_2O, PBS, or cell culture medium containing 10% FBS.

Cell viability

For viability studies, cells were seeded in a 96 well plate at 1000 cells/well and allowed to adhere for at least 3 h. The cells were dosed with various nanoconstructs in a final volume of 100 μl and incubated for 3 d (5% CO_2, 37°C, 100% humidity). After incubation cell viability was assessed using CCK-8 assay (Dojindo, Japan) and the difference in absorbance between 450 nm and 650 nm was used as the metric. For *in vitro* photothermal experiments, 25 pM AuNC@PDA or AuNC@PDA-Ax was incubated with the cells overnight, after the cells had been allowed to adhere for 3 h. Cells were washed twice with fresh media prior to irradiation by a diode laser (0.75 W, 808 nm); following irradiation cells were incubated for 72 h before viability was assessed. All viability assays were normalised to untreated cells within the same experiment, and biological triplicates were performed.

Migration assay

A six-well plate was seeded with 4T1 cells and allowed to become confluent. A total of 5 non-overlapping scratches were made using a 200 μL pipette tip. The media was

immediately aspirated and replaced with 0.5% FBS containing media followed by treatment with PBS, 20 μg/mL Ax, or 25 pM AuNC@PDA or AuNC@PDA-Ax. The wound was monitored for 72 h, and the width of the wound was measured using ImageJ (National Institute of Health, Bethesda, MD) at three spots per wound at various time points.

Inductively coupled plasma mass spectrometer

Each cell type was seeded at 20,000 cells per well in a 24-well plate and allowed to adhere overnight. AuNC@PDA (100 pM) or AuNC@PDA-Ax (4, 20, 100 pM) were added to wells and incubated for 2 h. Ax at 12 μM was preincubated for 5 min for use as a blocking agent. All samples were generated in triplicate. Cells were trypsinized, subjected to several freeze thaw cycles, digested with aqua regia and diluted to a final volume of 10 ml in 18 MΩ H_2O (final concentration 3% HCl, 1% HNO_3). For tissue, Balb/c mice averaging 6–8 weeks of age (Jackson Labs, ME) were inoculated subcutaneously in the rear limb with 1×10^5 4T1 cells. After 10 days, tumours had grown to an average size of 8–10 mm at which time the animal was injected intravenously via the tail vein with 0.1 pmol AuNC@PDA or AuNC@PDA-Ax ($N = 3$ per group). Tumours were harvested 24 h after injection and digested at 90 °C in 0.5 ml HNO_3 (99.999%) and 0.1 ml H_2O_2 (30%) overnight. After digestion, 0.25 ml HCl (99.999%) was added; the solution was diluted to 15 ml and filtered using a 70 μm cell strainer (Fisher). ICP-MS was performed using iCAP Q (Thermo). Argon was used as a carrier gas at a flow rate of 1.05 ml/min, and the fluid flow of 0.97 ml/min. The matrix alone was run between samples to reduce sample carryover. Immediately prior to analysis, calibration standards between 0.1 and 100 ppb Au (1 mg/mL stock, ULTRA Scientific) were prepared by serial dilution and run.

Darkfield imaging

Cells were seeded at 6×10^4 cells/well in an eight chamber slide (LabTek, Electron Microscopy Sciences, Hatfield, PA). Cells were allowed to adhere overnight and then incubated with different formulations for 3 h (10 pM AuNC) on a rocker. Cells were then washed four times with PBS and fixed with 100% ethanol (1 h, – 20°C). Cells were rinsed, mounting medium was added, and a cover slip was affixed with nail polish. Darkfield imaging was carried out using an Olympus IX81 microscope (Olympus Inc, Center Valley, PA) with a cytoviva darkfield condenser (Cytoviva Inc, Auburn, AL), halogen illumination, and a 20 × objective. Images were captured using an integrated Olympus DP72 camera.

Photoacoustic-fluorescence flow cytometry

For PA and fluorescence flow cytometry, 4T1 cells were seeded at 10^5 cells/well in a 24-well plate overnight then dosed with 20 pM of various nanoparticle formulations. Samples were allowed to incubate for up to 4 h, washed with PBS, then stained with rhodamine b isothiocyanate, trypsinized, collected by centrifugation, fixed with paraformaldehyde (2%, 20 min, 4°C), and washed three times with PBS. Details regarding the flow cytometry system can be found in the supporting information.

Photoacoustic mapping

For PA mapping, 10^5 4T1 cells were seeded in a one chamber slide (LabTek) or a 35 mm dish with coverslip bottom overnight. Media was removed and fresh media was added. Cells were then dosed with AuNCs at 20 pM for 2 h on a rocker. After incubation, the media was removed. Cells were stained with Hoechst 33342 stain for 20 min. The stain was removed, and cells were washed twice with PBS (2% FBS). Cells were then fixed with 2% paraformaldehyde (20 min, 4°C). The paraformaldehyde was removed, and the cells were washed twice with PBS; then a thin layer of personal lubricant (Walgreen's) was added to reduce Brownian motion. Details regarding the PA mapping system can be found in the supporting information.

Ex vivo studies

Balb/c mice averaging 6–8 weeks of age (Jackson Labs, Bar Harbor, ME, USA) were inoculated subcutaneously in the rear limb with 4×10^5 4T1 cells. After 8–10 days, tumours grew to an average size of 8–10 mm at which time the animal was euthanized and the tumour tissue was excised and frozen in OCT mounting medium. Sections of 5 μm thickness were prepared using a cryostat and affixed AuNC to glass slides. The tissue was fixed with acetone, rehydrated with PBS, and blocked for 30 min with 5% bovine serum albumin in PBS. Then the sections were stained with the 2.5 pM (in 5% BSA) for 1 h followed by three washes with PBS. A chamber was mounted to the slide and filled with DI H_2O to provide acoustic coupling during PA mapping.

Results

Synthesis and characterization of nanoconstructs

The three-step procedure used to generate the nanoconstructs is illustrated schematically in Figure 1; AuNCs were synthesised, coated with PDA, and conjugated with Ax for use in targeting galectin-1 expressing cells. AuNCs were successfully synthesised using the galvanic replacement method [52]. Based on TEM measurements, the AuNCs had an average exterior edge length of 39±3 nm and an interior edge length of 28 ± 3nm (Figure S1). The LSPR maximum appeared at 753 nm and had an extinction coefficient of ~1×10^{10} cm^{-1} M^{-1}. Based on analysis by ICP-MS, these AuNCs were determined to be 81% Au and 19% Ag by mass.

Dopamine was autopolymerised on the AuNC surface under basic, aerobic (pH = 9, 1 atm O_2) conditions. The reaction progress was monitored using UV-vis spectroscopy (Figure 2(A), Figure S2). The peak at 410 nm indicates the formation of the quinone intermediate [53], and the shift in the LSPR was monitored as a proxy for coating thickness. Aliquots were removed at 0, 30, 60, and 90 min (Figure 2(B–E)) incubation to assess the progress of the reaction, and the organic layer became thicker and denser as the reaction proceeded. For the following studies the reaction was quenched at 60 min, corresponding to an LSPR of ~770 nm.

Ax was conjugated to the surface *via* Michael addition. Various AuNC@PDA concentrations were incubated with 100 μg/mL Ax in borate buffer overnight. The AuNC@PDA-Ax was

isolated by centrifugation, and the protein concentration of the supernatant was quantified using the Bradford Assay (Figure 3(A)). These data indicated a maximum conjugation of ~5.8×10^4 Ax/AuNC based on the linear portion of the curve. This conjugation efficiency indicates 100 pM AuNC@PDA-Ax contains 5.8 μM Ax (~21 μg/mL), which is well below IC_{50}'s reported for murine endothelial cells (>75 μM) [54]. The hydrodynamic diameter as measured by nanoparticle tracking analysis increased from 126 nm to 135 nm following Ax conjugation. Colloidal stability was assessed in H_2O, PBS, and cell culture medium (Figure 3(B)). AuNC@PDA showed a negligible decrease in extinction in any medium. Conversely, AuNC@PDA-Ax suspensions had no extinction after 24 h in H_2O or PBS. In cell culture medium, 60% of the Ax-conjugated particles remained suspended after 24 h, and the settled particles were easily redispersed by inverting the cuvette.

Darkfield imaging was used to qualitatively confirm the targeting capacity of the Ax moiety due to the high scattering cross-section of the AuNC (Figure 3(C–F)). It was found that much greater cell binding occurred when high ratios of Ax and AuNCs were used. Additionally, AuNC@PDA and AuNC@PDA-Ax were incubated for 2 h with tumour and endothelial cells, harvested, and the Au in each sample was quantified by ICP-MS (Figure 3(G)). Without targeting, a degree of non-specific binding was observed at 100 pM. With Ax as a targeting agent, increasing the dose from 4 to 20 to 100 pM resulted in roughly five-fold increases in particles associated with cells with each increasing concentration. Interestingly, the 2H11 (endothelial) cells had more associated particles on average than the 4T1 (tumour) cells. When the cells were pre-incubated for 5 min with 12 μM free Ax, (twice the Ax dose contained in 100 pM AuNC@PDA-Ax), the number of bound particles per cell declined by ~80 and ~95% in 4T1 or 2H11 cells, respectively.

Cell viability and photothermal treatment

Alone, these formulations were found to have an ED_{50} (effective dose to kill 50% of cells) greater than 100 pM AuNC in both cancer (4T1) and endothelial (2H11) cell lines (Figure 4(A)). Conjugation of Ax did not result in a significant change to the ED_{50}. Cells were incubated overnight with 25 pM AuNC@PDA-Ax and treated photothermally with a diode laser (808 nm, 800 mW, ~$2W/cm^2$) after several washing cycles to remove unbound particles. Cell viability was assessed after three days (Figure 4(B)). Neither laser irradiation alone (20 min) nor treatment with particles in the absence of irradiation resulted in significant loss of cell viability in either cell type. Similarly, 20min irradiation after incubation with untargeted AuNC@PDA only resulted in ~15% reduction in cell viability. However, incubation with AuNC@PDA-Ax combined with 10 min irradiation resulted in ~60% reduction in viability, while 20 min irradiation resulted in a 90% reduction of viable tumour cells. Endothelial cells showed a 35% and 65% reduction in viability following 10 and 20 min irradiation, respectively. A thermocouple was used to determine the temperature of a well containing 25 pM AuNC@PDA-Ax in media without cells; after 30 min irradiation the temperature remained <40 °C. The ineffectiveness of the untargeted AuNC@PDA and the low bulk solution temperature of AuNC@PDA-Ax suggest that the targeted construct delivered high nanoregional heating that induced cell death.

A wound healing assay was used to confirm the retention of Ax's biological activity (Figure 4(C–D)). Within 72 h, wounds without treatment or treated with AuNC@PDA had completely closed with similar closure rates. The width of the wound had decreased by ~50% in the presence of 20μg/mL Ax and ~30% in the presence of 20 pM AuNC@PDA-Ax (~4 μg/mL Ax) after 72 h, indicating the retention of the biological activity of Ax following conjugation.

Photoacoustic characterization

PA and fluorescence flow cytometry further confirmed binding of AuNC@PDA-Ax to 4T1 cells. A plateau of ~50% of cells being positive for AuNC@PDA-Ax was reached after 3 h incubation in serum-containing media (Figure 5(A)). No significant change in the percentage of cells with bound particles nor the amount of particles bound to cells on average was observed between two and five washes (Figure 5(B)).

PA scanning was used to semi-quantitatively visualise cells with particles associated. A schematic illustration of the PA mapping system can be found in Figure S5. After 18 h incubation (Figure 6(A) and (B)), significant adherence of particles to the tissue culture slide was observed, but AuNC@PDA without Ax showed little PA signal above the background in the cells, while most cells had bound particles when incubated with AuNC@PDA-Ax and showed a roughly 15-fold increase in PA signal amplitude, against the untargeted particle. The results of high-resolution, Z-stacked images showed that after 2 h incubation (Figure 6(D)) the targeted particles were bound to the cell surface, while untargeted particles showed no significant signal. These studies indicate a rapid and specific interaction between the tumour cells and the targeted particle.

Tumour studies

The ability of the construct to bind to the tumour was confirmed using 5 μm tumour histological sections that were incubated with AuNC@PDA (Figure 7(A)) or AuNC@PDA-Ax with ~600 Ax/AuNC (Figure 7(B)) or 60,000 Ax/AuNC (Figure 7(C)) for 1 h followed by PA mapping of the tissue. Corresponding plots of PA intensity can be found in Figure S6. Similar to the *in vitro* study, a weak PA signal was observed with AuNC@PDA that was effectively identical to the background signal from the nontumour region. Conjugation with ~600 Ax induced 14-fold higher mean signal intensity within the tumour as compared to the region outside it, and conjugation with 60,000 Ax led to an additional four-fold increase (Figure 7(D)) in background-corrected mean signal intensity. A very obvious and readily detectable increase in PA signal across the tumour section of the AuNC@PDA-Ax was observed despite an increase in non-specific adsorption to the slide surface. Additionally, tumour-bearing mice were given an i.v. injection of 0.1 pmol of AuNC@PDA or AuNC@PDA-Ax. Tumours were harvested after 24 h, digested, and the uptake of AuNCs was quantified using ICP-MS (Figure 7(E)). A threefold increase in Au uptake following Ax conjugation compared to non-targeted AuNCs was observed.

Discussion

These studies demonstrate the feasibility of targeting AuNCs to the solid tumour microenvironment via galectin-1 expression on endothelial and tumour cells in a murine breast cancer model. Significant photothermal killing of tumour and endothelial cells was observed (Figure 4) only after administering the targeted AuNC and exposing cells to NIR laser irradiation. Interestingly, in general the non-targeted nanocages had limited effect in any of our *in vitro* assays, highlighting the critical need for more than passive accumulation of nanomaterials in the tumour in order for specific therapeutic effects to be achieved. Our results suggest that Ax is a promising approach to overcome this limitation as demonstrated here by quantification of cellular uptake (Figure 3(G)) and tumour uptake (Figure 7(E)). Further, the bulk temperature in the irradiated wells remained less than 40°C for the entire 20 min irradiation with targeted or non-targeted nanocages, well below typical hyperthermic conditions. In this context the value of targeting the nanocages to the cells enabled a therapeutic response beyond what would be expected using conventional hyperthermia where average temperatures are typically just over 40°C. We surmise that the targeted nanomaterials were able to damage cells due to a marked, intense nanoregional heating around the bound AuNCs in the membrane or cytoplasm of the cells. Interestingly, the tumour cells showed somewhat lower particle uptake than the endothelial cells, but they showed a greater photothermal response. While it may be expected from our prior work and that of others that a galectin-1 targeted construct would preferentially bind to endothelial cells, unpublished data from our lab suggests that 2H11 cells are more resistant to hyperthermia than tumour cells, which may explain this somewhat paradoxical result. Ongoing work in our laboratory is centred on the addition of drug-loading to the platform, as the AuNC constructs have already been used to controllably release drugs within tumours photothermally [55,56]. Ultimately, we expect that effective tumour destruction could be obtained in lesions accessible to laser irradiation by virtue of superficial growth (such as in chestwall disease) or by interstitial laser approaches.

The optical and photothermal properties of the AuNC structure appear to be equal to or superior in many ways to other nanoparticle morphologies. The combination of the melanin-like PDA coating and the AuNC enable the system to function as a potent generator of PA signal, allowing for non-invasive detection of single particles in tissue or cell preparations. This was demonstrated in the current study when the PA detection was executed *in vitro* (Figure 6), by flow cytometry (Figure 5), or *ex vivo* in histological sections of similar tumours (Figure 7). One of the more exciting aspects of targeted nanomedicines is the promise of obtaining a truly theranostic agent – one that can detect where the tumour is while simultaneously allowing therapy to be directed at it. Additionally, accumulation in the tumour can be monitored relatively easily, allowing the timing of the intervention to be optimised for maximum effect regardless of unique tumour pathophysiology. We surmise that our approach has merit in both of these aspects due to the detection sensitivity of the AuNC and its great capacity for heat generation upon absorption of near infra-red light [22]. When directed on or near the membrane of a galectin-1 expressing cell using the Ax peptide targeting strategy, this microheating gradient is enough to damage and kill cells. Our future studies are focussed on understanding the proper treatment sequences and doses for effective

solid tumour control *in vivo*, either by thermal damage alone or in combination with radiotherapy or chemotherapy-loaded nanocages.

Targeting galectin-1 is a promising approach as it is a widely expressed molecule present in and around the membrane of cells in a solid tumour. Breast tumours, pancreatic tumours, and multiple myeloma have all been shown to have up-regulated levels of galectin-1 [57–59]. Here, we demonstrate that even while bound to the AuNC, Ax at levels comparable to our previous work (2 μM or higher) [33] retains potent biological activity as evidenced by the marked inhibition of cell migration achieved (Figure 4). Additionally, cell association of the AuNCs can be competitively inhibited by co-incubating with free Ax. This suggests that our labelling strategy is not only feasible from a chemical synthesis standpoint, but that the peptide retains its normal biological activity and thus validates our approach with regard to the particle synthesis, PDA coating, and conjugation of the peptide. Overall, this new vehicle with dimensions of ~50 nm in its fully functional state and preferential ability to bind to and be a therapeutic effector in a model of metastatic breast cancer appears to be promising for improved nanomedicines against various solid malignancies.

An important consideration in the translation of nanomedicines from the bench to the clinic is the reproducibility of materials' biological effects. Certainly, considerations like cell lines and experimental procedures account for some of the variance in biological effects observed with nanomaterials reported by different labs. We observed consistent results across biological triplicates for our studies. Further, reproducible large scale synthesis of monodisperse AuNCs has been demonstrated by ourselves and others [52,60–62]. Additionally, many studies using AuNCs have shown little *in vivo* toxicity of the AuNCs alone [56,63] a major factor in developing any nanomedicine for clinical approval. The conjugation efficiency of Ax was reproducible when the same particle stock solution was used. The greatest source of heterogeneity is likely the PDA coating itself (as shown in Figure 2), which is unsurprising due to the variety of covalent and noncovalent interactions that hold the polymer together, though we can achieve low batch-to-batch variation. Indeed there continues to be great uncertainty as to the structure of the coating itself [64]. We are developing more robust and reproducible synthetic routes to improve the homogeneity of the polymer coating within each batch. Use of this type of system is particularly appealing as a nanomedicine because the high photothermal conversion efficiency of the AuNC allows a low dose of both laser energy and AuNCs to be used. Similarly, the high reproducibility and high synthetic yield of these materials make them appealing as therapeutic agents with realistic potential for further development.

Conclusions

In this report, we demonstrate the use of the anti-angiogenic peptide Ax as a targeting agent for PDA-coated AuNCs, and the retention of the peptide's biological activity was confirmed. While the targeted and non-targeted constructs by themselves had limited toxicity at identical concentrations, application of laser irradiation resulted in a significant decrease in viability for both tumour and endothelial cells only with the targeted nanocages. Targeting was confirmed *in vitro* using darkfield microscopy, PA microscopy, PA flow cytometry, and ICP-MS. We were further able to use the PA system to confirm targeting to tumour tissue

and initial in vivo biodistribution studies resulted in a three-fold increase in retention of the targeted nanocage compared to the nontargeted nanocage. This platform represents a promising route for targeting the vasculature as well as the tumour cells for multimodal detection and treatment of various cancers. In the future, this potent photothermal-therapeutic platform can potentially be further multiplexed with targeted chemotherapy delivery or radiotherapy and combined with a variety of image-guided approaches for personalised treatment.

Supplementary Material

Refer to Web version on PubMed Central for supplementary material.

Acknowledgments

We thank Prof. M.S. Smeltzer, PhD for supplying the diode laser for these studies. We also thank E. Pollack and B. Shaulis for help with the ICP-MS study at the Arkansas Mass Spectrometry facility, which is supported by the Arkansas Biosciences Institute.

Funding

This research was supported in part by a grant from the Arkansas Breast Cancer Research Programs and the Winthrop P. Rockefeller Cancer Institute, as well as by NIH grants R01CA131164 and R01EB017217, NSF grants OIA 1457888 and DBI 1556068, and the Translational Research Institute at UAMS.

References

1. [last accessed 31 Jul 2016] Pilot Study of AuroLase (tm) Therapy in Refractory and/or Recurrent Tumors of the Head and Neck. 2008–2014. Available from: https://clinicaltrials.gov/ct2/show/NCT00848042
2. [last accessed 31 Jul 2016] Efficacy Study of AuroLase Therapy in Subjects With Primary and/ or Metastatic Lung Tumors. 2012–2014. Available from: https://www.clinicaltrials.gov/ct2/show/NCT01679470
3. Libutti SK, Paciotti GF, Byrnes AA, et al. Phase I and pharmacokinetic studies of CYT-6091, a novel PEGylated colloidal gold-rhTNF nanomedicine. Clin Cancer Res. 2010; 16:6139–49. [PubMed: 20876255]
4. Anselmo AC, Mitragotri S. A review of clinical translation of inorganic nanoparticles. AAPS J. 2015; 17:1041–54. [PubMed: 25956384]
5. Dreaden EC, Alkilany AM, Huang X, et al. The golden age: gold nanoparticles for biomedicine. Chem Soc Rev. 2012; 41:2740–79. [PubMed: 22109657]
6. Jenkins, SV., Muldoon, TJ., Chen, J. Plasmonic nanostructures for biomedical and sensing applications. In: Xiong, Y., Lu, X., editors. Metallic Nanostructures: from controlled synthesis to applications. Switzerland: Springer International Publishing; 2015. p. 133-173.
7. Kobayashi H, Watanabe R, Choyke PL. Improving conventional enhanced permeability and retention (EPR) effects; what is the appropriate target? Theranostics. 2013; 4:81–9. [PubMed: 24396516]
8. Wilhelm S, Tavares AJ, Dai Q, et al. Analysis of nanoparticle delivery to tumours. Nat Rev Mater. 2016; 1:16014. http://www.nature.com/articles/natrevmats201614#supplementary-information.
9. Huang X, Peng X, Wang Y, et al. A reexamination of active and passive tumor targeting by using rod-shaped gold nanocrystals and covalently conjugated peptide ligands. ACS Nano. 2010; 4:5887–96. [PubMed: 20863096]
10. Chattopadhyay N, Fonge H, Cai Z, et al. Role of antibody-mediated tumor targeting and route of administration in nanoparticle tumor accumulation in vivo. Mol Pharm. 2012; 9:2168–79. [PubMed: 22734589]

11. Sykes EA, Dai Q, Sarsons CD, et al. Tailoring nanoparticle designs to target cancer based on tumor pathophysiology. Proc Natl Acad Sci USA. 2016; 113:E1142. [PubMed: 26884153]
12. De Jong WH, Hagens WI, Krystek P, et al. Particle size-dependent organ distribution of gold nanoparticles after intravenous administration. Biomaterials. 2008; 29:1912–19. [PubMed: 18242692]
13. Albanese A, Tang PS, Chan WC. The effect of nanoparticle size, shape, and surface chemistry on biological systems. Annu Rev Biomed Eng. 2012; 14:1–16. [PubMed: 22524388]
14. Sykes EA, Chen J, Zheng G, Chan WC. Investigating the impact of nanoparticle size on active and passive tumor targeting efficiency. ACS Nano. 2014; 8:5696–706. [PubMed: 24821383]
15. Bazak R, Houri M, El Achy S, et al. Cancer active targeting by nanoparticles: a comprehensive review of literature. J Cancer Res Clin Oncol. 2015; 141:769–84. [PubMed: 25005786]
16. Oyewumi MO, Yokel RA, Jay M, et al. Comparison of cell uptake, biodistribution and tumor retention of folate-coated and PEG-coated gadolinium nanoparticles in tumor-bearing mice. J Control Release. 2004; 95:613–26. [PubMed: 15023471]
17. Wolfe T, Chatterjee D, Lee J, et al. Targeted gold nanoparticles enhance sensitization of prostate tumors to megavoltage radiation therapy in vivo. Nanomed: Nanotechnol Biol Med. 2015; 11:1277–83.
18. Zelasko-Leon DC, Fuentes CM, Messersmith PB. MUC1-targeted cancer cell photothermal ablation using bioinspired gold nanorods. PLoS One. 2015; 10:e0128756. [PubMed: 26147830]
19. Meeker DG, Jenkins SV, Miller EK, et al. Synergistic photo-thermal and antibiotic killing of biofilm-associated *Staphylococcus aureus* using targeted antibiotic-loaded gold nanoconstructs. ACS Infect Dis. 2016; 2:241–50. [PubMed: 27441208]
20. Chen J, Glaus C, Laforest R, et al. Gold nanocages as photothermal transducers for cancer treatment. Small. 2010; 6:811–17. [PubMed: 20225187]
21. Chen J, Wang D, Xi J, et al. Immuno gold nanocages with tailored optical properties for targeted photothermal destruction of cancer cells. Nano Lett. 2007; 7:1318–22. [PubMed: 17430005]
22. Robinson R, Gerlach W, Ghandehari H. Comparative effect of gold nanorods and nanocages for prostate tumor hyperthermia. J Control Release. 2015; 220:245–52. [PubMed: 26526969]
23. Lisunova M, Dunklin JR, Jenkins SV, et al. The unusual visible photothermal response of free standing multilayered films based on plasmonic bimetallic nanocages. RSC Adv. 2015; 5:15719–27.
24. Liu X, Cao J, Li H, et al. Mussel-inspired polydopamine: a biocompatible and ultrastable coating for nanoparticles in vivo. ACS Nano. 2013; 7:9384–95. [PubMed: 24010584]
25. Hong S, Kim KY, Wook HJ, et al. Attenuation of the in vivo toxicity of biomaterials by polydopamine surface modification. Nanomedicine (Lond). 2011; 6:793–801. [PubMed: 21793672]
26. Cui J, Yan Y, Such GK, et al. Immobilization and intracellular delivery of an anticancer drug using mussel-inspired polydopamine capsules. Biomacromolecules. 2012; 13:2225–8. [PubMed: 22792863]
27. Ye Q, Zhou F, Liu W. Bioinspired catecholic chemistry for surface modification. Chem Soc Rev. 2011; 40:4244–58. [PubMed: 21603689]
28. Folkman J. Tumor angiogenesis: therapeutic implications. N Engl J Med. 1971; 285:1182–6. [PubMed: 4938153]
29. Denekamp J. Endothelial cell proliferation as a novel approach to targeting tumour therapy. Br J Cancer. 1982; 45:136–9. [PubMed: 7059456]
30. Wagner SC, Ichim TE, Ma H, et al. Cancer anti-angiogenesis vaccines: is the tumor vasculature antigenically unique? J Translat Med. 2015; 13:340.
31. Garcia-Barros M, Paris F, Cordon-Cardo C, et al. Tumor response to radiotherapy regulated by endothelial cell apoptosis. Science. 2003; 300:1155–9. [PubMed: 12750523]
32. Berbeco RI, Ngwa W, Makrigiorgos GM. Localized dose enhancement to tumor blood vessel endothelial cells via mega-voltage X-rays and targeted gold nanoparticles: new potential for external beam radiotherapy. Int J Radiat Oncol Biol Phys. 2011; 81:270–6. [PubMed: 21163591]

33. Dings RP, Williams BW, Song CW, et al. Anginex synergizes with radiation therapy to inhibit tumor growth by radiosensitizing endothelial cells. Int J Cancer. 2005; 115:312–19. [PubMed: 15688384]
34. Denekamp J. Vascular attack as a therapeutic strategy for cancer. Cancer Metastasis Rev. 1990; 9:267–82. [PubMed: 2292139]
35. Koonce NA, Quick CM, Hardee ME, et al. Combination of gold nanoparticle-conjugated tumor necrosis factor-alpha and radiation therapy results in a synergistic antitumor response in murine carcinoma models. Int J Radiat Oncol Biol Phys. 2015; 93:588–96. [PubMed: 26461001]
36. Visaria RK, Griffin RJ, Williams BW, et al. Enhancement of tumor thermal therapy using gold nanoparticle-assisted tumor necrosis factor-alpha delivery. Mol Cancer Ther. 2006; 5:1014–20. [PubMed: 16648573]
37. Peiris PM, Deb P, Doolittle E, et al. Vascular targeting of a gold nanoparticle to breast cancer metastasis. J Pharm Sci. 2015; 104:2600–10. [PubMed: 26036431]
38. Shao J, Griffin RJ, Galanzha EI, et al. Photothermal nanodrugs: potential of TNF-gold nanospheres for cancer theranostics. Sci Rep. 2013; 3:1293. [PubMed: 23443065]
39. Thijssen VL, Postel R, Brandwijk RJ, et al. Galectin-1 is essential in tumor angiogenesis and is a target for antiangiogenesis therapy. Proc Natl Acad Sci USA. 2006; 103:15975–80. [PubMed: 17043243]
40. Rabinovich GA. Galectin-1 as a potential cancer target. Br J Cancer. 2005; 92:1188–92. [PubMed: 15785741]
41. Liu FT, Rabinovich GA. Galectins as modulators of tumour progression. Nat Rev Cancer. 2005; 5:29–41. [PubMed: 15630413]
42. Upreti M, Jamshidi-Parsian A, Apana S, et al. Radiation-induced galectin-1 by endothelial cells: a promising molecular target for preferential drug delivery to the tumor vasculature. J Mol Med (Berl). 2013; 91:497–506. [PubMed: 23090010]
43. Kuo P, Bratman SV, Shultz DB, et al. Galectin-1 mediates radiation-related lymphopenia and attenuates NSCLC radiation response. Clin Cancer Res. 2014; 20:5558–69. [PubMed: 25189484]
44. Dings RP, Van Laar ES, Loren M, et al. Inhibiting tumor growth by targeting tumor vasculature with galectin-1 antagonist anginex conjugated to the cytotoxic acylfulvene, 6-hydroxylpropylacylfulvene. Bioconjug Chem. 2010; 21:20–7. [PubMed: 20020769]
45. Dings RP, Van Laar ES, Webber J, et al. Ovarian tumor growth regression using a combination of vascular targeting agents anginex or topomimetic 0118 and the chemotherapeutic irofulven. Cancer Lett. 2008; 265:270–80. [PubMed: 18378392]
46. Griffin RJ, Koonce NA, Dings RP, et al. Microbeam radiation therapy alters vascular architecture and tumor oxygenation and is enhanced by a galectin-1 targeted anti-angiogenic peptide. Radiat Res. 2012; 177:804–12. [PubMed: 22607585]
47. Dings RP, van der Schaft DW, Hargittai B, et al. Anti-tumor activity of the novel angiogenesis inhibitor anginex. Cancer Lett. 2003; 194:55–66. [PubMed: 12706859]
48. Dings RP, Loren M, Heun H, et al. Scheduling of radiation with angiogenesis inhibitors Anginex and Avastin improves therapeutic outcome via vessel normalization. Clin Cancer Res. 2007; 13:3395–402. [PubMed: 17545548]
49. Dings RP, Yokoyama Y, Ramakrishnan S, et al. The designed angiostatic peptide anginex synergistically improves chemotherapy and antiangiogenesis therapy with angiostatin. Cancer Res. 2003; 63:382–5. [PubMed: 12543791]
50. Dings RP, Mayo KH. A journey in structure-based drug discovery: from designed peptides to protein surface topomimetics as antibiotic and antiangiogenic agents. Acc Chem Res. 2007; 40:1057–65. [PubMed: 17661438]
51. Dings RP, Arroyo MM, Lockwood NA, et al. Beta-sheet is the bioactive conformation of the anti-angiogenic anginex pep-tide. Biochem J. 2003; 23:281–8.
52. Skrabalak SE, Au L, Li X, Xia Y. Facile synthesis of Ag nanocubes and Au nanocages. Nat Protoc. 2007; 2:2182–90. [PubMed: 17853874]
53. Munoz JL, Garcia-Molina F, Varon R, et al. Calculating molar absorptivities for quinones: application to the measurement of tyrosinase activity. Anal Biochem. 2006; 351:128–38. [PubMed: 16476401]

54. van der Schaft DW, Dings RP, de Lussanet QG, et al. The designer anti-angiogenic peptide anginex targets tumor endothelial cells and inhibits tumor growth in animal models. FASEB J. 2002; 16:1991–3. [PubMed: 12397082]
55. Jenkins SV, Srivatsan A, Reynolds KY, et al. Understanding the interactions between porphyrin-containing photosensitizers and polymer-coated nanoparticles in model biological environments. J Coll Interf Sci. 2016; 461:225–31.
56. Srivatsan A, Jenkins SV, Jeon M, et al. Gold nanocage-photosensitizer conjugates for dual-modal image-guided enhanced photodynamic therapy. Theranostics. 2014; 4:163–74. [PubMed: 24465274]
57. Storti P, Marchica V, Airoldi I, et al. Galectin-1 suppression delineates a new strategy to inhibit myeloma-induced angiogenesis and tumoral growth in vivo. Leukemia. 2016; 30:2351–63. [PubMed: 27311934]
58. Dalotto-Moreno T, Croci DO, Cerliani JP, et al. Targeting galectin-1 overcomes breast cancer-associated immunosuppression and prevents metastatic disease. Cancer Res. 2013; 73:1107. [PubMed: 23204230]
59. Shen J, Person MD, Zhu J, et al. Protein expression profiles in pancreatic adenocarcinoma compared with normal pancreatic tissue and tissue affected by pancreatitis as detected by two-dimensional gel electrophoresis and mass spectrometry. Cancer Res. 2004; 64:9018. [PubMed: 15604267]
60. Jenkins SV, Gohman TD, Miller EK, Chen J. Synthesis of hollow gold-silver alloyed nanoparticles: a “galvanic replacement” experiment for chemistry and engineering students. J Che Educ. 2015; 92:1056–60.
61. Pang B, Yang X, Xia Y. Putting gold nanocages to work for optical imaging, controlled release and cancer theranostics. Nanomedicine. 2016; 11:1715–28. [PubMed: 27348546]
62. Piao J-G, Wang L, Gao F, et al. Erythrocyte membrane is an alternative coating to polyethylene glycol for prolonging the circulation lifetime of gold nanocages for photothermal therapy. ACS Nano. 2014; 8:10414–25. [PubMed: 25286086]
63. Fratoddi I, Venditti I, Cametti C, Russo MV. How toxic are gold nanoparticles? The state-of-the-art. Nano Res. 2015; 8:1771–99.
64. Liebscher J, Mrowczynski R, Scheidt HA, et al. Structure of polydopamine: a never-ending story? Langmuir. 2013; 29:10539–48. [PubMed: 23875692]

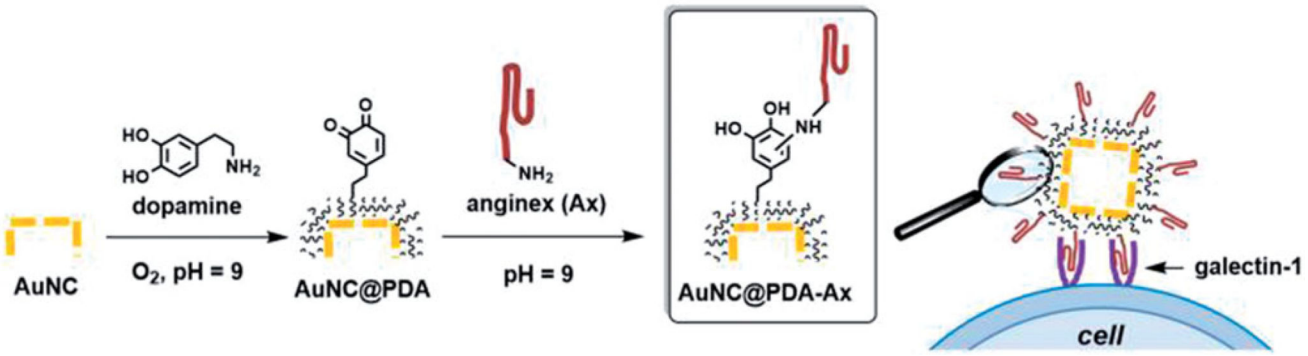

Figure 1.
Schematic illustration of the construction of AuNC@PDA-Ax and its biological action. Not to scale.

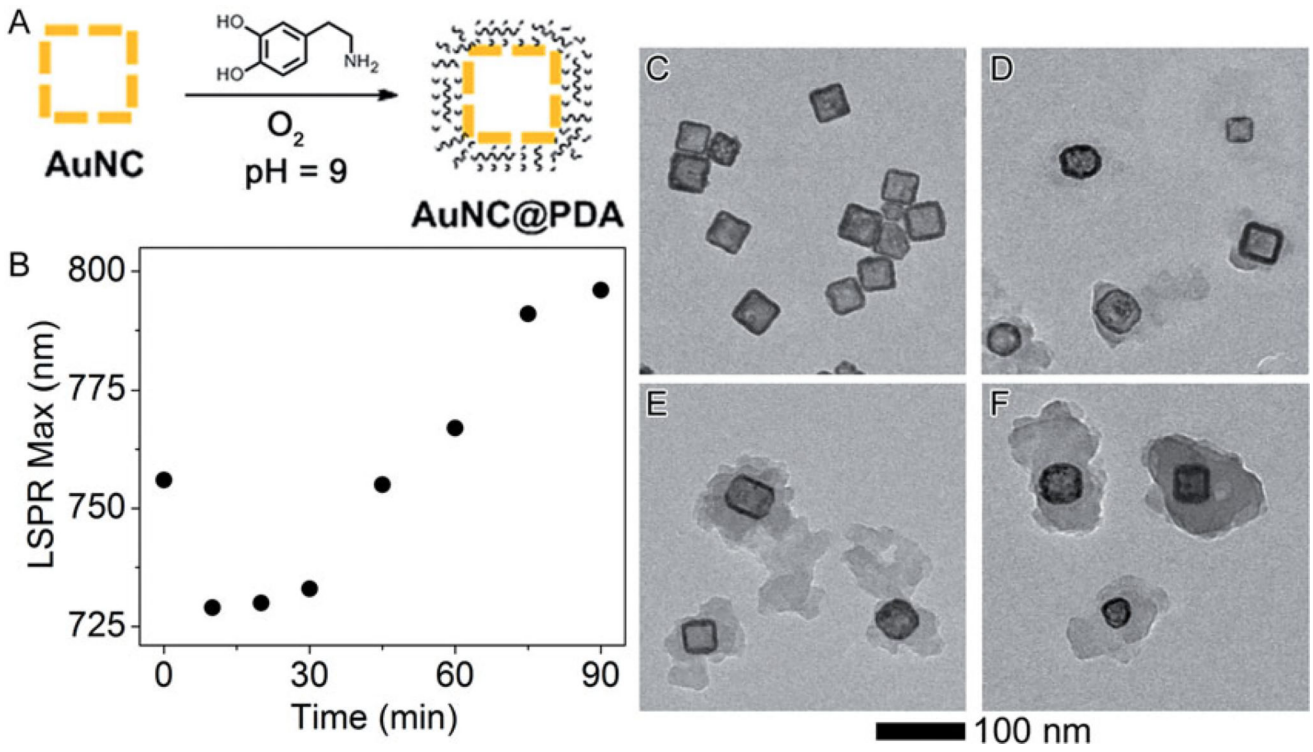

Figure 2.

Synthesis and characterisation of PDA layer. (A) Scheme of polymerization (B) LSPR maximum as a function of reaction time. Original spectra can be found in Figure S2; representative TEM images of AuNC@PDA after the reaction had proceeded for different time periods: (C) 0 min, (D) 30 min, (E) 60 min and (F) 90 min.

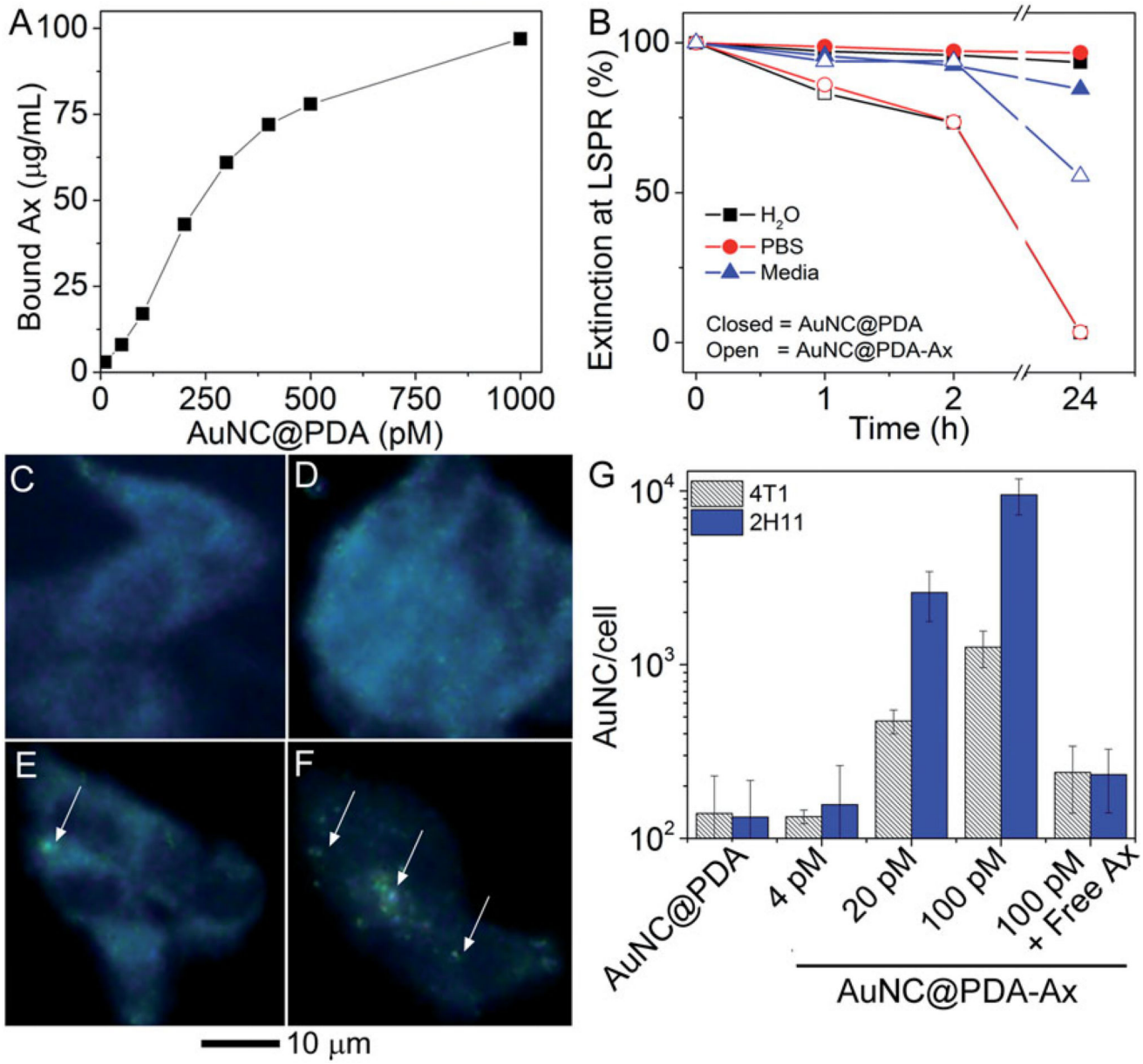

Figure 3.

Anginex (Ax) is present on the AuNCs and enables *in vitro* association with tumour cells. (A) Bound Ax as a function of AuNC@PDA concentration; (B) colloidal stability of AuNC@PDA and AuNC@PDA-Ax in various media; typical darkfield images of 4T1 cells incubated with (C) no treatment, (D) AuNC@PDA, and AuNC@PDA-Ax with (E) ~ 10^2 or (F) ~ 10^4 Ax/AuNC@PDA, arrows indicate cell-bound particles; and (G) ICP-MS quantification of AuNC per cell following 2 h incubation where the "100 pM + free axe" represents a blocking study using 2:1 ratio of free Ax to particle bound Ax.

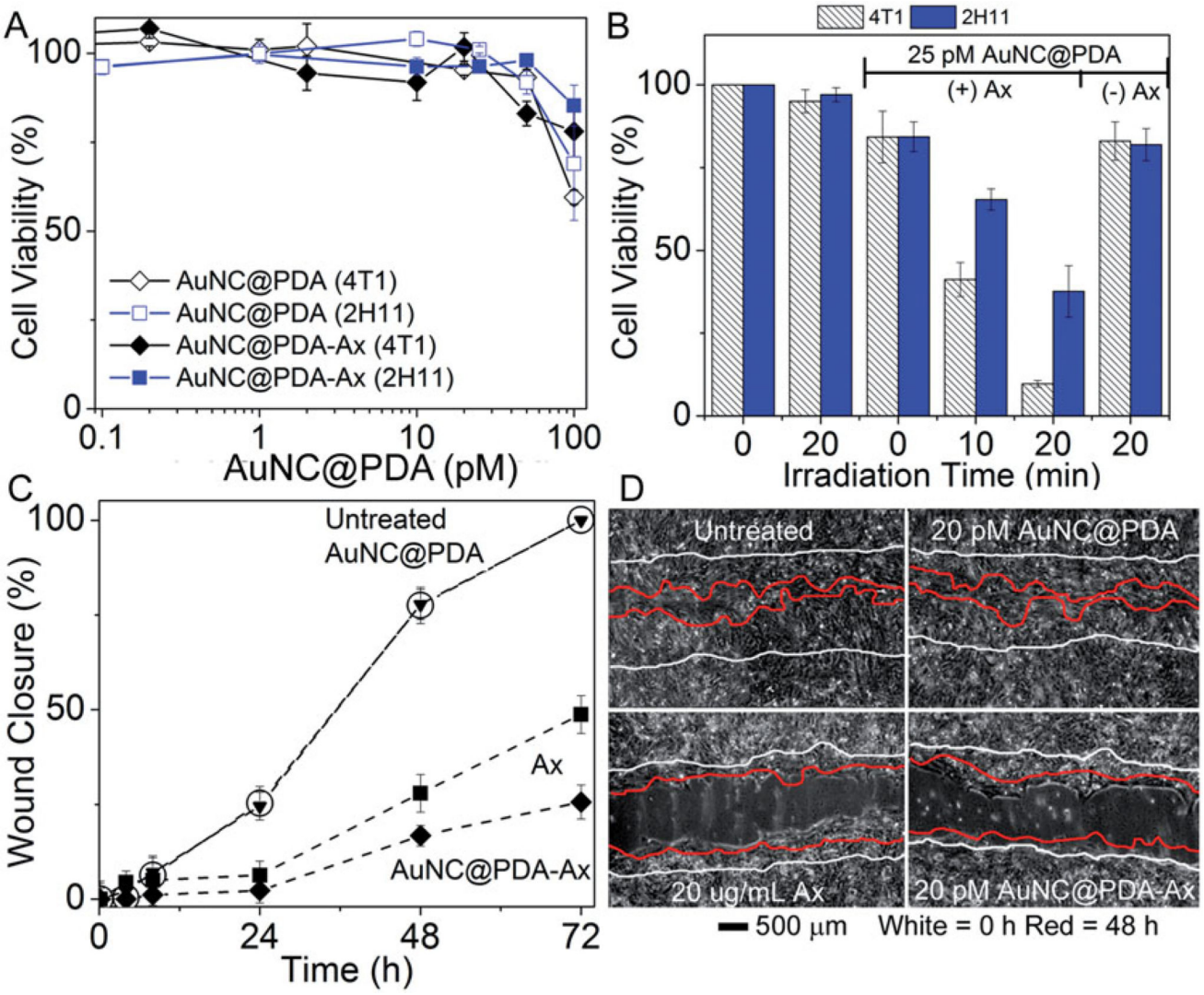

Figure 4.

Nanocages have low toxicity alone while only targeted nanocages induce supra-additive photothermal killing and block functional ability of cells to migrate. (A) Viability of (squares) 4T1 and (diamonds) 2H11 in the absence of laser irradiation under increasing (open) AuNC@PDA or (filled) AuNC@PDA-Ax concentrations normalised to untreated cells; (B) cell viability during photothermal experiments for (striped) 4T1 and (solid) 2H11 cell lines normalised to untreated cells; (C) migration assay of 4T1 cells that were (circles) untreated or treated with (triangles) 20 pM AuNC@PDA, (squares) 20 μg/mL Ax, or (diamonds) 20 pM AuNC@PDA-Ax; (D) Representative images of the wound after 72h, with 0h traced in white and 48h traced in red. Viability assays are result of three independent experiments and error bars represent SEM.

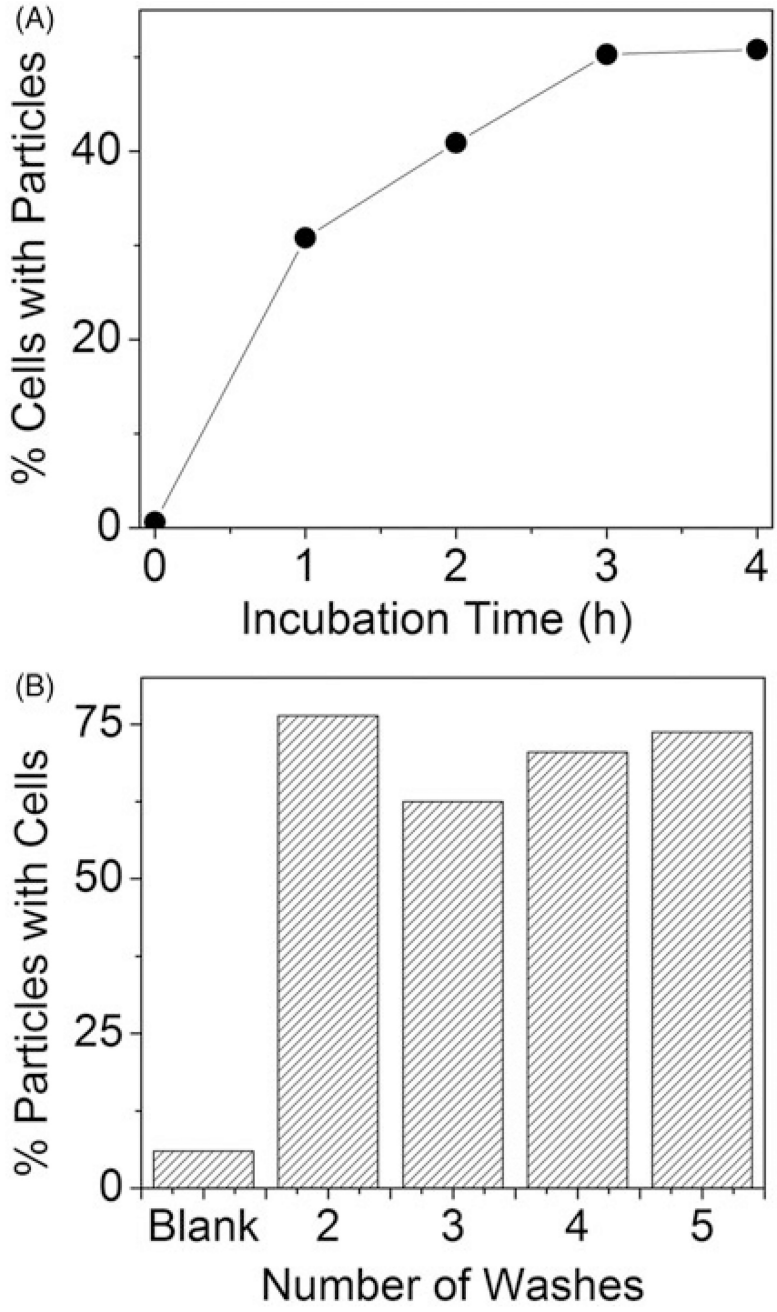

Figure 5.

PA flow cytometry reveals strong association of targeted AuNCs with 4T1 tumour cells. (A) Percentage of PA positive cells as a function of incubation time with 25 pM Ax-conjugated AuNCs. (B) Particles bound to cells as a function of washes presented as per cent of AuNC PA signal with simultaneous rhodamine (non-specific cell stain) fluorescence signal.

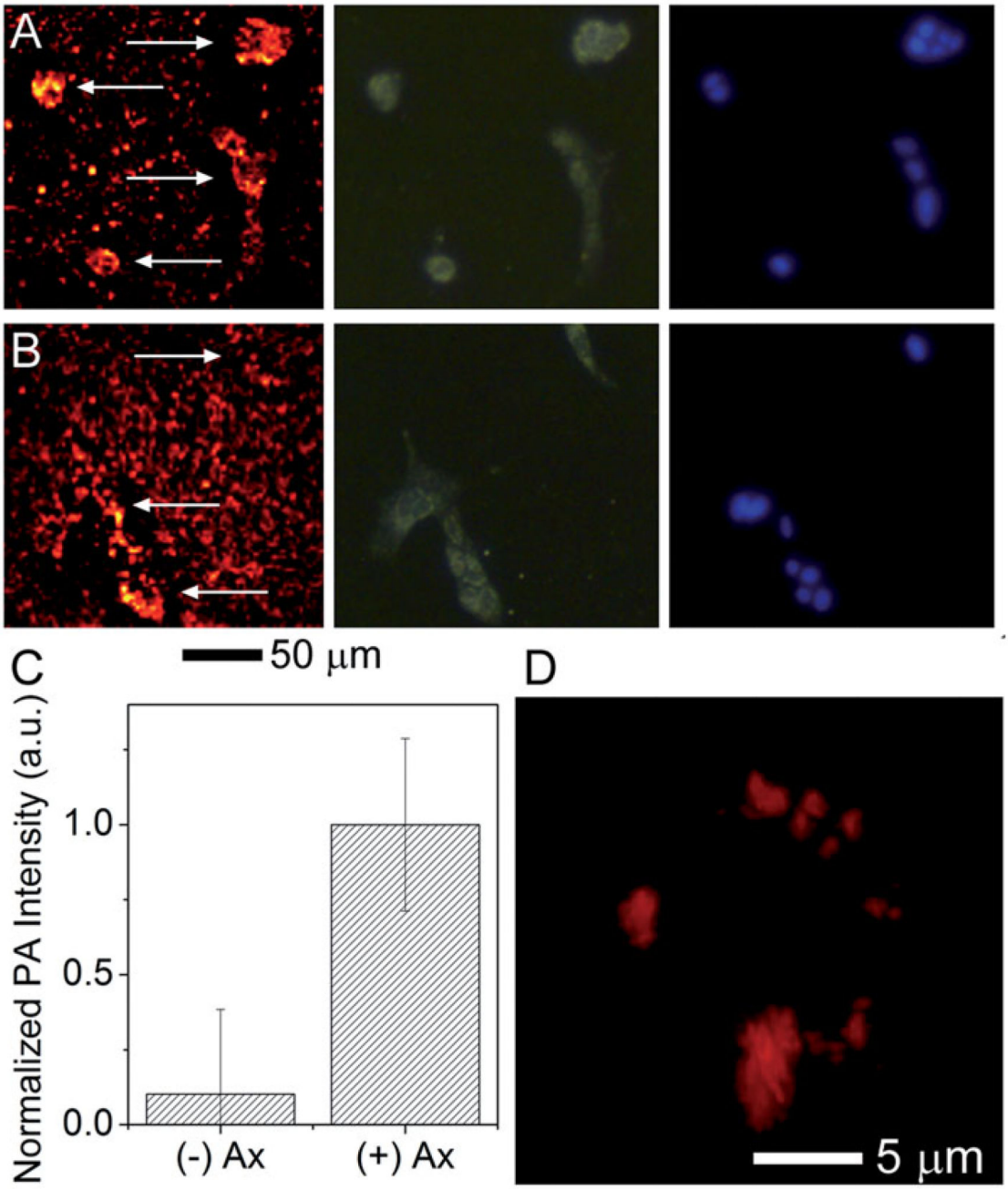

Figure 6.

Multimodality imaging of cells and associated nanocages. 4T1 cells were incubated with (A) AuNC@PDA-Ax or (B) AuNC@PDA for 18 h and stained with DAPI. The same area was imaged via (left) PA, (centre) scattering, and (right) fluorescence microscopy arrows in the PA image are used to denote the location of cells; (C) background corrected quantification of photoacoustic signal associated with cells (n= 30), error bars show SEM; and (D) 3 D reconstruction of the PA signal of a typical 4T1 cell incubated with AuNC@PDA-Ax for 2h demonstrating widespread surface binding of the construct by this time point taken using a 60 × objective.

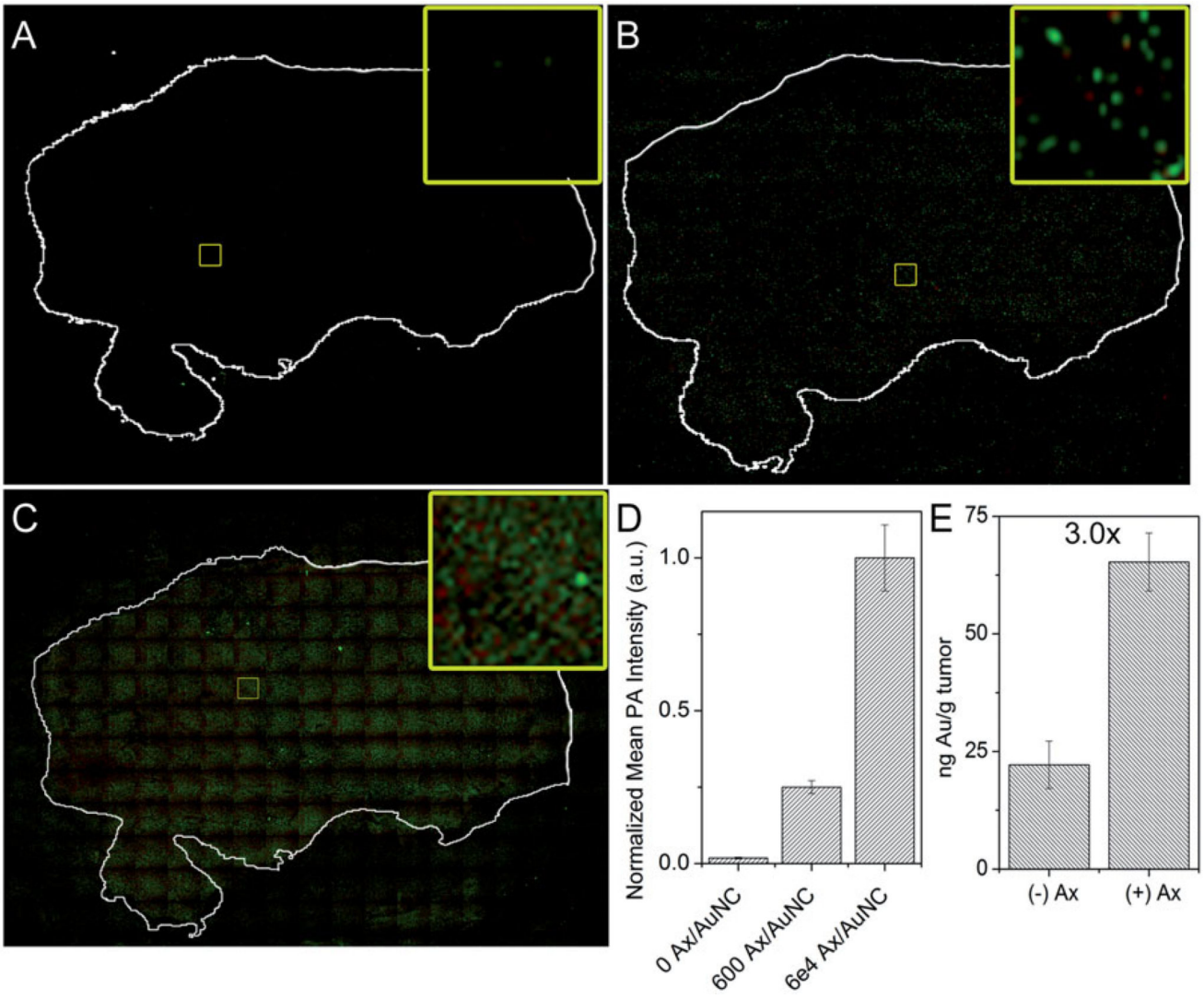

Figure 7.

Ex vivo tumour targeting. PA mapping of sequential 4T1 tumour sections from a single tumour stained with either (A) AuNC@PDA, (B) AuNC@PDA-Ax (600 Ax/AuNC), or (C) AuNC@PDA-Ax (60,000 Ax/AuNC) as detected with photoacoustic mapping. Green shows high intensity pixels, red shows low intensity pixels, and black shows no signal. Tumour sections were stained with crystal violet and the outline overlaid and shown in white. Inset shows only the photoacoustic signal from a representative region. (D) Quantification of mean background corrected PA intensity from 20 arbitrary regions within each tumour section. (E) ICP-MS quantification of 4T1 tumour uptake of AuNC@PDA and AuNC@PDA-Ax 24h after i.v. administration of 0.1 pmol of each preparation.